

A 64 Channel 3T Array Coil for Highly Accelerated Fetal Imaging at 22 Weeks of Pregnancy

by

Mark H. Spatz

Submitted to the Department of Electrical Engineering and Computer
Science

in partial fulfillment of the requirements for the degree of
Master of Engineering in Electrical Engineering and Computer Science

at the

MASSACHUSETTS INSTITUTE OF TECHNOLOGY

February 2017

© Massachusetts Institute of Technology 2017. All rights reserved.

Author
Department of Electrical Engineering and Computer Science
Feb 3, 2017

Certified by
Lawrence L. Wald
Professor of Radiology, Harvard Medical School
Thesis Supervisor

Accepted by
Christopher Terman
Chairman, Masters of Engineering Thesis Committee

A 64 Channel 3T Array Coil for Highly Accelerated Fetal Imaging at 22 Weeks of Pregnancy

by

Mark H. Spatz

Submitted to the Department of Electrical Engineering and Computer Science
on Feb 3, 2017, in partial fulfillment of the
requirements for the degree of
Master of Engineering in Electrical Engineering and Computer Science

Abstract

MRI is an attractive tool for fetal imaging due to its unique ability to provide detailed anatomical and physiological data in an inherently safe manner. In practice, the problem of unpredictable and nonrigid fetal motion limits fetal MRI to fast single shot T2 weighted sequences such as HASTE, which have poor tissue contrast, low SNR, and cannot provide detailed physiological information. In this work, we designed, built, and tested a semi-adjustable anatomically shaped 64 channel array coil for fetal imaging at 22 weeks of pregnancy. The coil's performance was compared to that of the vendor's standard configuration consisting of an 18 channel flexible body array and 16 channels from a 32 channel spine array. The fetal coil provides roughly 5% better SNR in the fetal brain region of an anthropomorphic phantom and allows increasing SENSE acceleration factor from $R = 4$ to $R = 5$ in the right-left direction and $R = 3$ to $R = 4$ in the head-foot direction.

Thesis Supervisor: Lawrence L. Wald
Title: Professor of Radiology, Harvard Medical School

Acknowledgments

I would like to thank, in order:

- My parents Jeff and Nancy, for catapulting me into a life wherein I've had the opportunity to pursue an advanced degree at MIT.
- Larry Wald and Elfar Adalsteinsson, the professors who introduced me to the world of medical imaging and provided me with this opportunity inside of it.
- Pablo García-Polo, who designed the majority of the 3D printed parts for the fetal array, including all of the coil formers and covers, and who designed and built the stunningly detailed pregnant abdomen phantom that has enabled the testing of this array. He is the architect of the fetal coil project.
- The residents of the RF lab, whose expertise, assistance, and camaraderie made the completion of this work possible: Boris Keil, Jason Stockmann, Chris Lapierre, Azma Mareyam, Chis Ha, Charlotte Sappo, and all the rest.
- Jonathan Polimeni, for the use of his Matlab scripts in generating SNR and g-factor maps.
- The Muddy Charles Pub, both as an institution and as a collection of people.
- The staff of the student center Anna's.
- The developers of Debathena.
- All the group chats (including the ones I'm not in).

Contents

1	Introduction	15
2	Background	17
2.1	Origin of MR signal	17
2.1.1	Nuclear Spins	17
2.1.2	Spins in the Presence of External Magnetic Fields	17
2.1.3	Spin Dynamics	19
2.1.4	Bloch Equation	20
2.2	Signal Equation	20
2.2.1	Signal Detection Through Faraday Induction	21
2.3	Fourier Encoding	22
2.3.1	Gradient Fields	22
2.3.2	The Fourier Transform	23
2.4	Noise in MRI	24
2.4.1	Thermal Noise	24
2.4.2	Preamp Noise	25
3	Array Design	29
3.1	Physical Design	29
3.2	Array Construction	29
3.3	Cable Traps	31
3.3.1	Helical Traps	31
3.3.2	Bazooka Trap	33

3.3.3	Trap Tuning	35
4	Loop Elements	37
4.1	Active Detuning	37
4.2	Passive Detuning	38
4.3	Loop Model	38
4.4	Complete Loop Circuit	40
4.5	Loop Circuit Analysis	40
4.6	Loop Component selection	41
4.6.1	Loop Circuit Considerations	41
4.6.2	Loop Resonance	42
4.6.3	Off resonance behavior	42
4.6.4	Optimal Component values	43
4.6.5	Verifying Optimal Component Values	44
5	Figures of Merit	47
5.1	Signal to Noise Ratio Maps	47
5.2	SENSE Geometry Factor	49
5.2.1	K-space Sampling for the 2DFT	49
6	Methods	53
6.1	Bench Tests	53
6.1.1	Intercoil Coupling and Reflection Coefficient Measurements . .	53
6.1.2	Loop Detuning and Preamp Decoupling Verification	53
6.2	MRI Data Acquisition and Reconstruction	54
7	Results	55
7.1	Covariance Weighted SNR Maps	55
7.2	Inverse G-Factor Maps	56
7.3	Noise Matrices	57
7.4	Per-Element SNR	60

List of Figures

2-1	Two port model of a noisy preamp connected to a noisy source.	26
3-1	Computer rendering of array panels and housings.	30
3-2	Finished coil, posed on 22 week pregnant abdomen phantom.	32
3-3	View of internal array construction and wiring.	33
3-4	Bazooka Balun before assembly.	34
3-5	Completed bazooka balun with open enclosure.	34
3-6	Cable trap with current injection probes.	35
4-1	Complete loop circuit schematic	39
4-2	Loop circuit models.	40
4-3	Loop impedances vs. frequency with optimal component values. . . .	45
7-1	Comparative covariance weighted SNR maps, transverse slice through fetal phantom brain.	55
7-2	Comparative covariance weighted SNR maps, coronal slice through fetal phantom brain.	56
7-3	Comparative covariance weighted SNR maps, sagital slice through fetal phantom brain.	56
7-4	Comparative inverse SENSE g-factor maps, transverse slice through fetal phantom brain, acceleration in right-left direction.	57
7-5	Comparative inverse SENSE g-factor maps, transverse slice through fetal phantom brain, acceleration in anterior-posterior direction. . . .	57

7-6 Comparative inverse SENSE g-factor maps, Coronal slice through fetal phantom brain, acceleration in right-left direction.	58
7-7 Comparative inverse SENSE g-factor maps, coronal slice through fetal phantom brain, acceleration in head-feet direction.	58
7-8 Comparative inverse SENSE g-factor maps, sagital slice through fetal phantom brain, acceleration in head-feet direction.	58
7-9 Comparative inverse SENSE g-factor maps, sagital slice through fetal phantom brain, acceleration in anterior-posterior direction.	59
7-10 Comparative inverse SENSE g-factor maps, coronal slice through fetal phantom brain, acceleration in head-feet, right-left directions.	59
7-11 Absolute value of noise covariance matrix ($ \Psi $).	60
7-12 Absolute value of inter-channel noise correlation coefficients ($ \sqrt{\text{diag}(\Psi)} ^{-1} \cdot \Psi \cdot \sqrt{\text{diag}(\Psi)} $).	61
7-13 Mean Single Element SNR values Inside the Fetal Phantom Brain (Top:Abdomen Panel and Side Wings, Bottom: Back panel)	62

List of Tables

4.1	Loop simulation parameters	45
4.2	Calculated optimal component values	45

Chapter 1

Introduction

MRI is increasingly used in addition to ultrasound to evaluate potential fetal disorders in routine clinical practice. Indeed, MRI provides a higher soft tissue contrast than ultrasound in the fetus and reproductive organs. MRI also has the potential to provide valuable physiological information through spectroscopic and diffusion weighted imaging. In practice, the problem of unpredictable and nonrigid fetal motion limits fetal MRI to fast single shot T2 weighted sequences such as HASTE, which have poor tissue contrast, low SNR, and cannot provide detailed physiological information.

High density arrays are needed to minimize acquisition times and maximize SNR. A standard fetal MRI protocol employs a spine array and a flexible body array to reach a total of approximately 34 channels. This limits the acceleration factors that can be achieved. Additionally, these general purpose coils are often unable to completely conform to the varied anatomy of pregnant patients, leaving some receive elements distant to the abdomen. In this work, we designed, built, and tested a semi-adjustable anatomically shaped 64 channel array coil for fetal imaging at 22 weeks of pregnancy on a 3T MAGNETOM Skyra system (Siemens Healthcare GmbH, Erlangen, Germany) .

Chapter 2

Background

In this chapter, I will lay out the basics of MR imaging and some of the considerations involved, loosely following themes in [5].

2.1 Origin of MR signal

2.1.1 Nuclear Spins

Spin is a quantum mechanical property that describes a particle's intrinsic angular momentum. Atoms with an odd number of protons or neutrons possess net nuclear spin, and therefore have mutually aligned angular momentum \vec{S} and magnetic dipole moment $\vec{\mu} = \gamma \vec{S}$, where γ is the gyromagnetic ratio: a known constant defined for every nucleus. Hydrogen (${}^1\text{H}$) is such an atom, having one proton and no neutrons. Along a given axis, hydrogen spins are quantized to $\pm \frac{\hbar}{2}$. Therefore, hydrogen dipole moments are likewise quantized to $\pm \gamma \frac{\hbar}{2}$ (eq. 2.1).

$$\mu = \pm \gamma \frac{\hbar}{2} \tag{2.1}$$

2.1.2 Spins in the Presence of External Magnetic Fields

In the presence of a strong polarizing field \vec{B}_0 pointing in the z direction and with magnitude B_0 , the potential energy of a spin with dipole moment $\vec{\mu}$ is the dot product

between the two vectors.

$$E = -\vec{\mu} \cdot \vec{B}_0 \quad (2.2)$$

Because μ is quantized, there is a gap ΔE between realizable energy states.

$$\Delta E = \gamma \hbar B_0 \quad (2.3)$$

Polarization

Spins tend to settle in the low energy state, pointing in the direction of \vec{B}_0 . However, at room temperature, thermal energy vastly exceeds the energy gap between the two states, and the ratio of spins aligned with \vec{B}_0 (n_+) to those anti aligned (n_-) is described by the Boltzmann distribution in eq. 2.4. For hydrogen ($\gamma = \frac{42.58 \text{ MHz}}{2\pi T}$) at room temperature ($T = 273K$) at a field strength of $3T$, $\Delta E = 5.283 \times 10^{-7} \text{ eV}$, and $\frac{n_-}{n_+} \approx (1 - 2.25 \times 10^{-5})$. This relatively tiny fraction of excess spin polarization is the source of the NMR signal. Luckily, there are 3.3428×10^{23} protons in a gram of water, resulting in 7.5×10^{18} aligned spins per gram under the previously stated conditions. Since living things tend to contain mostly water, the proposal of MRI is still promising.

$$\frac{n_-}{n_+} = \exp\left(-\frac{\Delta E}{kT}\right) = \exp\left(-\frac{\gamma \hbar B_0}{kT}\right) \quad (2.4)$$

In a large population of spins, the net magnetic dipole moment per unit volume is termed \vec{M} . In equilibrium, it is the product of the volumetric spin density N , the magnitude of a single spin dipole moment μ , and the excess fraction of aligned spins. It points in the same direction as \vec{B}_0 and has magnitude M_0 . Using the first two terms of a taylor series expansion of the Boltzmann distribution, we can approximate M_0 as eq. 2.5.

$$M_0 = N \cdot \mu \cdot (1 - \exp\left(-\frac{\Delta E}{kT}\right)) \approx \frac{N \gamma^2 \hbar^2 B_0}{2kT} \quad (2.5)$$

2.1.3 Spin Dynamics

In equilibrium, \vec{M} comes to point in the direction \vec{B}_0 with magnitude M_0 . But the next step will be to tip \vec{M} off of the z axis so that it has a component in the x - y plane. The observed behavior will then be time varying.

Precession

A single magnetic dipole $\vec{\mu}$ with mutually aligned angular momentum \vec{S} placed in an external magnetic field \vec{B} will experience a torque $\vec{\mu} \times \vec{B}$. Multiplying this torque by γ gives an expression for the time rate of change of $\vec{\mu}$, eq. 2.6. Eq. 2.6 shows $\vec{\mu}$ moving in a direction perpendicular to both itself and \vec{B} , i.e. precessing about \vec{B} . The frequency of this precession is ω_L in eq. 2.7.

$$\frac{d\vec{\mu}}{dt} = \vec{\mu} \times \gamma \vec{B} \quad (2.6)$$

$$\omega_L = \gamma \cdot B \quad (2.7)$$

A population of dipole moments precessing in synchrony gives a net magnetization \vec{M} that also precesses at ω_L .

Longitudinal Relaxation

Define the component of \vec{M} that is parallel to \vec{B}_0 as \vec{M}_z . In equilibrium $|\vec{M}_z| = M_0$, but immediately following the tipping of \vec{M} into the x - y plane by an angle α at time $t = 0$, \vec{M}_z is reduced to a value shown in eq. 2.8.

$$\vec{M}_z(t = 0+) = \cos(\alpha) \cdot \vec{M}_z(0-) \quad (2.8)$$

\vec{M}_z then begins to exponentially recover to its equilibrium magnitude of M_0 . The time constant associated with this longitudinal recovery is termed T_1 . T_1 is dependent on the tissue or material being imaged, but also has a positive dependence on B_0 field strength.

$$\vec{M}_z(t) = \hat{\mathbf{k}} M_0 + (\vec{M}_z(0+) - \hat{\mathbf{k}} M_0) \cdot \exp\left(-\frac{t}{T_1}\right) \quad (2.9)$$

Transverse Relaxation

Define the component of \vec{M} that is perpendicular to \vec{B}_0 as \vec{M}_{xy} . In equilibrium, $\vec{M}_{xy} = 0$. Immediately following the tipping of \vec{M} onto the x axis by an angle α at time $t = 0$, \vec{M}_{xy} is as shown in eq. 2.10. Individual spins begin to dephase as soon as they are tipped into the x - y plane, and so the net transverse magnetization \vec{M}_{xy} experiences exponential decay, as shown in eq. 2.11. The time constant associated with this transverse decay is termed T_2 , and is a property of the tissue or material being imaged.

$$\vec{M}_{xy}(t = 0+) = \hat{\mathbf{i}} \sin(\alpha) \cdot |\vec{M}_z(0-)| \quad (2.10)$$

$$\vec{M}_{xy}(t) = \vec{M}_{xy}(0+) \cdot \exp\left(-\frac{t}{T_2}\right) \quad (2.11)$$

2.1.4 Bloch Equation

Assembled together, the spin dynamics described above form the Bloch equation, shown in eq. 2.12. The complete Bloch equation describes the behavior of spins in a generalized external magnetic field \vec{B} that is the sum of the main field B_0 , the RF field B_1 , and the spatially varying gradient fields G .

$$\frac{d\vec{M}}{dt} = \vec{M} \times \gamma \vec{B} - \frac{M_x \hat{\mathbf{i}} + M_y \hat{\mathbf{j}}}{T_2} - \frac{(M_z - M_0) \hat{\mathbf{k}}}{T_1} \quad (2.12)$$

2.2 Signal Equation

The NMR signal arises from the precessing transverse component of the magnetization vector. As we begin to focus solely on \vec{M}_{xy} , I will follow the convention used by Nishimura [5] and define a new variable M that represents the transverse

magnetization as a function of location and time with single complex number.

$$M(\vec{r}, t) \equiv |\vec{M}_x| + j|\vec{M}_y| \quad (2.13)$$

2.2.1 Signal Detection Through Faraday Induction

The wire loop antenna is the most commonly used receive element in clinical MRI. It works by directly coupling to the field produced by the transverse magnetization of the sample under test. The precessing magnetization produces a time varying magnetic flux piercing the surface defined by the loop, which induces a voltage ϵ around the loop through Faraday induction.

$$\epsilon = -\frac{d\Phi_B}{dt} = -\frac{d}{dt} \iint_A B(\vec{r}, t) dA \quad (2.14)$$

A loop antenna has spatially varying sensitivity to spins. If a unit current through the loop produces a field \vec{B}_1 at location \vec{r} in the sample, then magnetization \vec{M} at that location produces a flux of $\vec{B}_1 \cdot \vec{M}$ through the loop. [2]. Citing linearity, we can find an expression for the total voltage induced around the loop by summing the individual contributions from every location in the sample volume.

$$\epsilon = -\frac{d}{dt} \iiint_V \vec{B}_1(\vec{r}) \cdot \vec{M}(\vec{r}) d\vec{r} \quad (2.15)$$

The voltage around the loop depends on the time derivative of a volume integral over the entire sample volume. At this point, it is clear why only the precessing transverse magnetization is of interest for signal detection. Substituting our complex variable M into eq. 2.15, and replacing \vec{B}_1 with a more general complex sensitivity function $C(\vec{r})$ that also accounts for spatially dependent signal phase, we get the beginnings of the signal equation

$$\epsilon = -\frac{d}{dt} \iiint_V C(\vec{r}) \cdot M(\vec{r}, t) d\vec{r} \quad (2.16)$$

2.3 Fourier Encoding

2.3.1 Gradient Fields

Spatial encoding in traditional MRI is achieved by applying spatially varying gradient fields on top of the main field, as shown in eq. 2.17. Just like \vec{B}_0 , \vec{G} points in the \hat{k} direction. Unlike \vec{B}_0 , \vec{G} varies as a function of space and time.

$$\vec{B} = (B_0 + G(\vec{r}, t))\hat{k} \quad (2.17)$$

After an initial flip resulting in a spatial magnetization distribution $M(\vec{r}, t = 0)$, spins begin precess under the influence of G , as described in 2.18. After a time t , spins at a location \vec{r} have accrued excess phase in proportion to the time integral of $G(\vec{r}, t)$.

$$M(\vec{r}, t) = M(\vec{r}, t = 0)e^{-j\gamma B_0 t} \exp(-j\gamma \int_0^t G(\vec{r}, \tau) d\tau) \quad (2.18)$$

Plugging this expression for M into eq. 2.16, making the assumption that $B_0 \gg G$ so that all spins precess at a frequency of approximately $\omega_L = \gamma B_0$, and dividing by $e^{-j\omega_L t}$ to downconvert to baseband, we extend the signal equation to describe the effect of gradient fields.

$$s(t) = -j\omega_L \iiint_V C(\vec{r}) M(\vec{r}, t = 0) \exp(-j\gamma \int_0^t G(\vec{r}, \tau) d\tau) \quad (2.19)$$

If we constrain ourselves to linear encoding gradients, such that

$$G(\vec{r} = x\hat{i} + y\hat{j} + z\hat{k}, t) = G_x(t)x + G_y(t)y + G_z(t)z \quad (2.20)$$

and then define three k variables to describe the history of G along each axis:

$$\begin{aligned}
k_x &= \frac{\gamma}{2\pi} \int_0^t G_x(\tau) d\tau \\
k_y &= \frac{\gamma}{2\pi} \int_0^t G_y(\tau) d\tau \\
k_z &= \frac{\gamma}{2\pi} \int_0^t G_z(\tau) d\tau
\end{aligned} \tag{2.21}$$

we come up with the final form of the signal equation:

$$s(t) = -j\omega_L \iiint_V C(\vec{r}) M(\vec{r}, t = 0) e^{-jk_xx} e^{-jk_yy} e^{-jk_zz} dV \tag{2.22}$$

2.3.2 The Fourier Transform

The Fourier transform breaks down a function into its individual frequency components by taking inner products of that function with complex exponential. Its one dimensional form is shown in eq. 2.23.

$$F(k_x) = \int_{-\infty}^{\infty} f(x) e^{-j2\pi k_x x} dx \tag{2.23}$$

Strikingly, eqs. 2.22 and 2.23 look extremely similar. The effect of our carefully chosen linear gradient fields has been to set up a physical three dimensional Fourier transform, where we take the inner product of M with a complex exponential whose phase has a linear dependence on space. Manipulation of $G(t)$ allows us to visit and sample arbitrary coordinates (k_x, k_y, k_z) in so called "k-space". By collecting k-space points on a Cartesian grid and obeying certain sampling criteria, we can collect data that directly represents a spatial Fourier transform of the sample under test, weighted by $C(\vec{r})$ and $M(\vec{r}, t = 0+)$.

2.4 Noise in MRI

2.4.1 Thermal Noise

The signals involved in MRI are very weak, and extreme care is taken to avoid and minimize all possible noise sources. Thermal noise arising inside the body is, however, unavoidable. When a perfectly conducting wire loop is brought near an object with finite conductivity, inductive coupling causes a transformed resistance R_{LOAD} to appear in the loop. R_{LOAD} depends on the geometry and conductivity of the object that is loading the loop, as well as the strength of the coupling. If R_{LOAD} is measurable, it can be used to quantify the thermal noise voltage that will be detected.

$$\bar{e_n^2} = 4kT_{LOAD}R_{LOAD}\Delta f \quad (2.24)$$

If all components of the MR setup are well designed, this innate noise source will dominate over all others.

Estimating R_{LOAD}

A current I flowing in the loop creates a spatially varying magnetic field $\vec{B}_1(\vec{r})$ in the sample below it. If I is sinusoidal, then the changing \vec{B}_1 will create an associated electric field \vec{E} according to Faraday's law of induction.

$$\nabla \times \vec{E}(\vec{r}) = -\frac{\partial \vec{B}_1(\vec{r})}{\partial t} \quad (2.25)$$

If we can solve for this \vec{E} , and if we know the conductivity of the sample, we can determine the power deposition in the sample and model it by R_{LOAD} .

$$P_{SAMPLE} = \frac{1}{2} \iiint_V \sigma |\vec{E}(\vec{r})|^2 d\vec{r} \quad (2.26)$$

$$R_{LOAD} = \frac{P_{SAMPLE}}{I^2} \quad (2.27)$$

2.4.2 Preamp Noise

Of the noise sources that we can control, the first amplifier in the signal processing chain is most critical. By faithfully amplifying the weak NMR signal early, the relative impact of noise injected by further transmission and processing steps is lessened. Here, I follow chapter 10.6 of [4] to derive an optimal source admittance that optimizes the noise performance of an amplifier.

Noise Factor

Noise factor (denoted by F) is a parameter that characterizes the noise performance of an amplifier (or mixer, or any other signal processing block). It is defined as:

$$F = \frac{\text{Total Output Noise Power}}{\text{Output Noise Power Due To Source}} \quad (2.28)$$

In systems consisting of multiple blocks (preamplifier, analog filter, mixer, ADC..) it becomes useful to refer to the logarithm of F , so that the noise contribution of cascaded blocks can be represented as a sum. This logarithmic parameter is called noise figure:

$$NF = 20 \log_{10}(F) \quad (2.29)$$

Two Port Noise Model

A two port model of a noisy amplifier is shown in figure 2-1. The noise behavior of the amplifier is completely characterized by two input referenced noise sources: a voltage source with mean value \bar{e}_n , and a current source with mean value \bar{i}_n .

Connected to the input of the amplifier is a noise current source with input admittance Y_S and mean value \bar{i}_s . The input noise current is assumed to arise purely from the real part of Y_S , so the two are related by eq. 2.30

$$Re(Y_S) = G_S = \frac{\bar{i}_s^2}{4kT\Delta f} \quad (2.30)$$

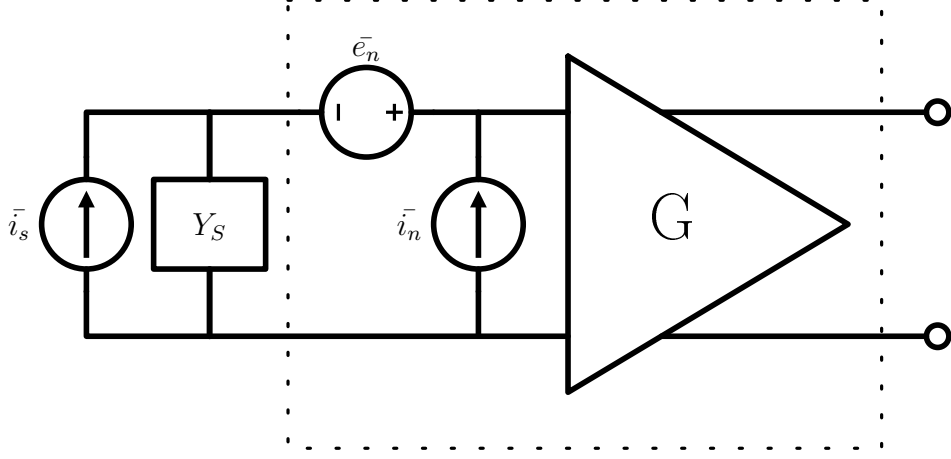


Figure 2-1: Two port model of a noisy preamp connected to a noisy source.

We assume that i_s^- statistically independent from e_n^- and i_n^- , since they arise inside of physically distinct devices. Since e_n^- and i_n^- may arise inside of a single transistor, they cannot be assumed to be uncorrelated.

Using the parameters of this model, we can begin to calculate the amplifier's noise figure. Since we only need to find the ratio between total noise power and source derived noise power, not the actual values themselves, we can use the short cut that output power will be proportional to short circuit mean square input current in both cases.

$$F = \frac{\bar{i}_s^2 + |i_n + Y_S e_n|^2}{\bar{i}_s^2} \quad (2.31)$$

If we expand the squared term in the numerator, we can get rid of cross terms between uncorrelated variables:

$$F = \frac{\bar{i}_s^2 + |i_n + Y_S e_n|^2}{\bar{i}_s^2} \quad (2.32)$$

The next step is to break up i_n into two parts: i_{n_u} which is uncorrelated with e_n , and i_{n_c} which is completely correlated to e_n . The correlation coefficient takes the form of a complex transadmittance Y_C , as it is a ratio between a current and a voltage.

$$i_n = i_{n_u} + i_{n_c} = i_{n_u} + Y_C e_n \quad (2.33)$$

Making this substitution and again removing uncorrelated cross terms, eq. 2.32 becomes:

$$F = 1 + \frac{\bar{i}_u^2 + |Y_S + Y_C|^2 \bar{e}_n^2}{\bar{i}_s^2} \quad (2.34)$$

Admittance, Conductivity, and Susceptibility

Before beginning the next section, recall that just as a complex impedance Z can be decomposed into its real resistance R and imaginary reactance X , a complex admittance Y may be decomposed into a conductivity G and susceptance B :

$$\begin{aligned} Z &= R + jX \\ Y &= G + jB \end{aligned} \quad (2.35)$$

Optimal Source Admittance

There is an optimal value Y_S that will minimize F . All that's left to do in finding it is to set up 2.34 so that we can take derivatives with respect to Y_S and set them equal to zero.

Replace the admittances Y_S and Y_C with the corresponding conductivities and susceptances, then substitute $\bar{i}_s^2 = G_S 4kT \Delta f$ in the denominator. eq. 2.34 becomes:

$$F = 1 + \frac{\bar{i}_u^2 + [(G_C + G_S)^2 + (B_C + B_S)^2] \bar{e}_n^2}{4kT \Delta f G_S} \quad (2.36)$$

Minimize F with respect to B_S :

$$\frac{\partial F}{\partial B_S} = \frac{(2B_C + 2B_S) \bar{e}_n^2}{4kT \Delta f G_S} \implies B_{S_{OPT}} = -B_C \quad (2.37)$$

Then, minimize F with respect to G_S and plug in $B_{S_{OPT}}$:

$$\frac{\partial F}{\partial G_S} = -\frac{i_u^2 + e_n^2 [G_C^2 + (B_C + B_S)^2]}{4kT\Delta f {G_S}^2} + \frac{e_n^2}{4kT\Delta f} \implies G_{S_{OPT}} = \sqrt{\frac{i_u^2}{e_n^2} + G_C^2} \quad (2.38)$$

We have found our optimal source impedance $Y_{S_{OPT}}$.

$$Y_{S_{OPT}} = \sqrt{\frac{i_u^2}{e_n^2} + G_C^2 - jB_C} \quad (2.39)$$

Chapter 3

Array Design

3.1 Physical Design

The 22 week fetal array is designed to provide good surface area coverage and close physical fit on a range of body types at 22 weeks of pregnancy. It consists of a rigid posterior panel that attaches directly to the patient table and a group of anterior and lateral panels that can be freely positioned on the patient. The two lateral panels are attached to the anterior panel with hinges to provide a degree of freedom. The patient facing surfaces of these panels are modeled after segmented images of a 22 weeks pregnant volunteer. The precise geometry of the hinged panel assembly was arrived at through iterative fit tests on pregnant volunteers.

The coil formers and housings were designed in Rhinoceros (Robert McNeel & Associates, WA, USA) and printed in poly carbonate on a Fortus 400mc 3D printer (Stratasys, Ltd., MN, USA).

3.2 Array Construction

The array consists of four distinct groups of coil elements. The posterior panel contains 24 loops, each with a diameter of approximately 9cm . The anterior panel contains 20 loops, with a median loop diameter of 8cm and with several outliers in the non-hexagonally tiled area. The two lateral panels contain 10 7cm loops each. The

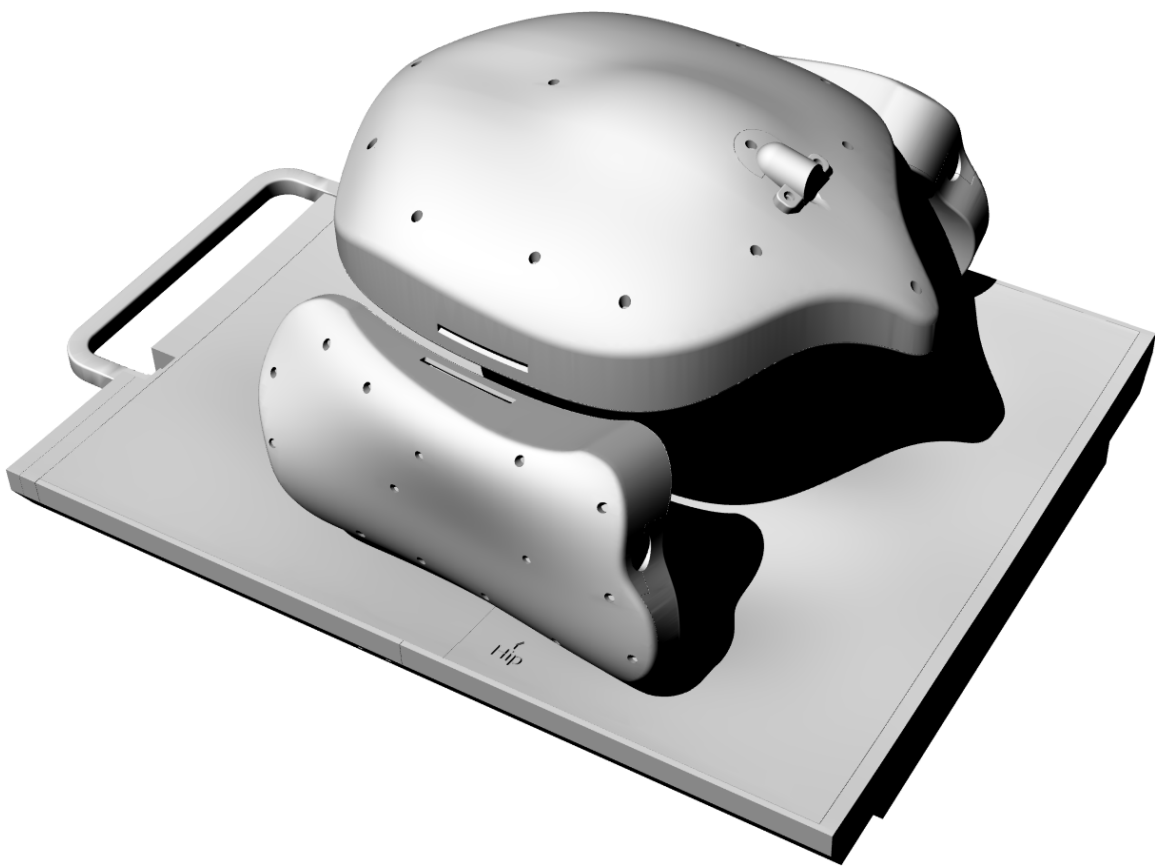


Figure 3-1: Computer rendering of array panels and housings.

loops in each panel are for the most part arranged in a hexagonal tiling pattern that allows each loop to be critically overlapped with all of its neighbors, thus minimizing inductive coupling between neighboring loops [8]. The loop layout is shown in detail in 7-13.

Individual loops were constructed from 16 gauge tin plated copper wire, with bridges bent into the wires to allow them to cross each other without touching. A schematic of the loop circuitry is shown in 4-1. Chapter 4 contains a detailed explanation of the function of the loop circuit.

The finished coil is shown in figure 3-2 posed on the pregnant abdomen phantom used extensively in testing. A view of the internal construction and wiring is shown in figure 3-3.

3.3 Cable Traps

Precautions must be taken to prevent large common mode currents from developing on internal and external wiring during the RF transmit phase. Such uncontrolled currents could pose a fire/safety hazard, and at the very least would interfere with the sequence being run. Common mode chokes spaced every 20cm on all internal and external prevent the induced currents from growing too large. Due to the high magnetic field the array operates in, ferrite chokes are not an option. Instead, tuned resonant traps are constructed. Two types of traps were used in this array.

3.3.1 Helical Traps

The operation of the resonant helical traps visible in fig. 3-3 is easy to understand. The jacketed wire bundle is wound around a helical former to create an air core inductor. High voltage capacitors are then connected across the turns of the inductor, forming a parallel LC tank. At resonance, the trap presents a high impedance to common mode currents flowing in the jacket. This kind of trap can hold off hundreds of volts, and has a high Q. It is used as the first cable trap inside each array panel, and inside the foot end table plug.



Figure 3-2: Finished coil, posed on 22 week pregnant abdomen phantom.

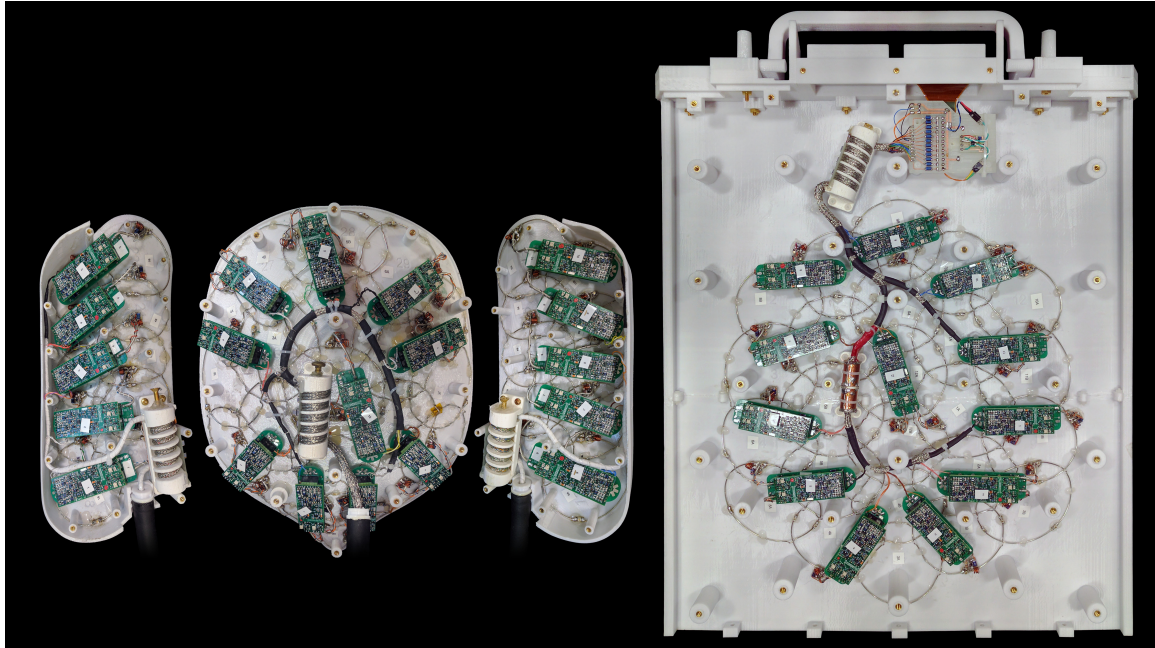


Figure 3-3: View of internal array construction and wiring.

3.3.2 Bazooka Trap

The bazooka trap can be thought of as a physically short bazooka balun that has been electrically lengthened to $\frac{\lambda}{4}$ by shunting the open end with a capacitor. A cylindrical plastic spacer is printed in two halves. The outside surface of each half is covered in copper tape, with a gap left in the middle. The two halves are placed around the wire bundle and soldered together, and each end of the balun is soldered to the braided wire jacket. The gap in the copper tape is bridged with nonmagnetic capacitors selected such that the structure resonates at the desired frequency. An additional layer of copper shielding on the balun enclosure stabilizes the capacitance between the two ends of the balun so that external loading does not affect its resonant frequency. This kind of trap is more compact and consumes less wire length than the helical trap, but cannot hold off as much voltage and has a lower Q. It is placed periodically on long runs of external wiring.

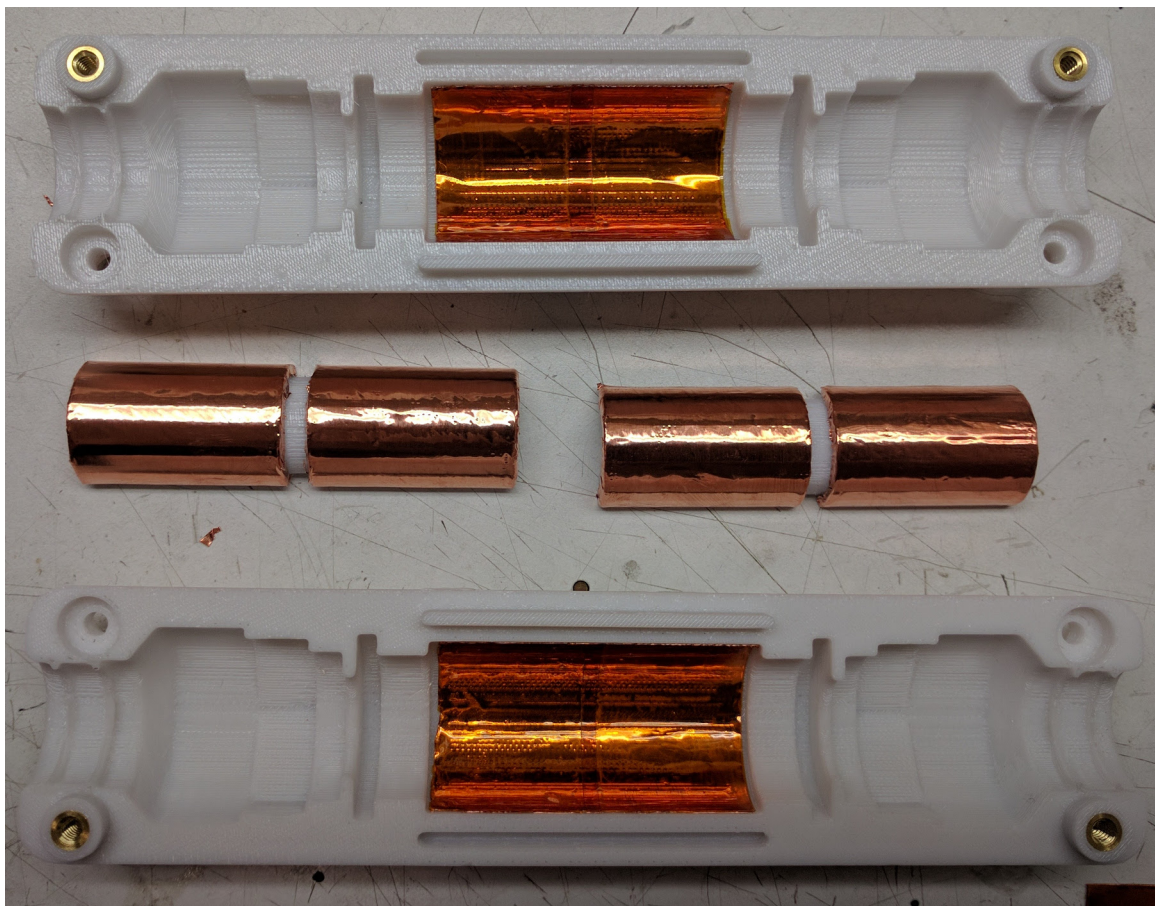


Figure 3-4: Bazooka Balun before assembly.

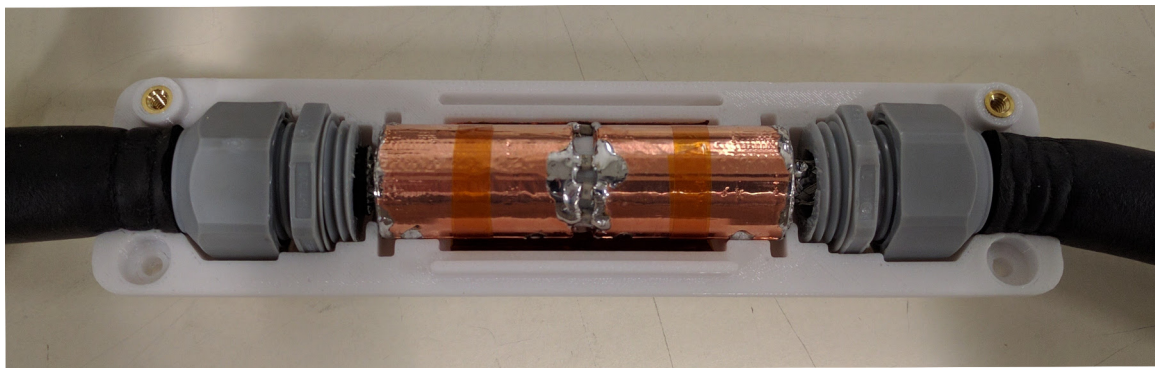


Figure 3-5: Completed bazooka balun with open enclosure.



Figure 3-6: Cable trap with current injection probes.

3.3.3 Trap Tuning

Both of the cable trap types described are narrow band, and must be properly tuned to function. This is accomplished through the use of a network analyzer and two current injection probes (fig. 3-6). Under the right measurement conditions, a prominent dip ($20dB$) in $|S_{12}|$ around the resonance frequency can be observed.

Chapter 4

Loop Elements

The same basic loop circuit, shown in figure 4-1, is duplicated 64 times to create the full array. The components appearing inside the dashed green box exist on a small FR4 circuit board termed the "feed point board." Here, I will discuss the purpose and function of each part of this circuit. All capacitors used in the loop circuit are Voltronics Series 11 non-magnetic.

4.1 Active Detuning

The loop is a resonant circuit that is strongly coupled to the volume surrounding it. It is necessary to spoil this resonance during the high power RF transmit pulses so that excessive currents are not induced in the loop. Such unintended energy deposition could adversely affect transmit homogeneity, damage the array, or create a safety hazard. Selective detuning is achieved by switching an inductor across one of the loop capacitors, creating a parallel resonant tank that behaves as an open circuit in the loop at ω_L .

A DC bias current of about $120mA$ is injected on the line marked BIAS in figure 4-1. This bias current flows through a PIN diode D_1 (MACOM MA47461F-1072), creating an RF short and effectively switching L_{TRAP} across C_{S3} . L_{TRAP} is an adjustable air core inductor, and is hand tuned to resonate with C_{S3} at precisely ω_L . The parallel resonant circuit thus formed creates a virtual open circuit in the loop,

preventing current from circulating in the loop. As soon as the bias current is removed and the diode recovers, the trap is disabled and the loop once again becomes tuned. The Q of this active detuning trap is kept high by using a relatively high value high Q inductor for L_{TRAP} . In this case, we used a $60nH$ hand wound inductor made with 16 AWG enameled copper wire.

The bias current is injected through a bias tee formed by L_{BIAS} ($3.3uH$ Coilcraft) and a $1nF$ capacitor to prevent leakage or injection of RF signal from/to the loop on the bias line.

4.2 Passive Detuning

The active detuning strategy is sufficient for assurance of image quality and protection from hardware damage, but a passive method is required to ensure patient safety in the event of an electrical failure. The crossed diode pair D_2 (BAV99) clamps the voltage across C_{S3} and L_{TRAP} to safe levels, passively enabling the trap if the energy stored in the loop gets too high. Other designs might also include RF fuses in the loop circuit, but the loops employed in this array are all small enough that this was not necessary.

4.3 Loop Model

The essence of the wire loop receive elements used in this array is a damped series resonant circuit, shown in figure 4-2A. The loop has a distributed inductance by nature of its geometry, and is broken at regular intervals by discrete capacitors. Wire and component resistances and (more importantly) inductive coupling to adjacent conductive materials reduces the loop Q to a finite value. This effect is modeled by a series resistor with value $R_{LOAD} = \sqrt{\frac{L}{C}} \cdot \frac{1}{Q}$

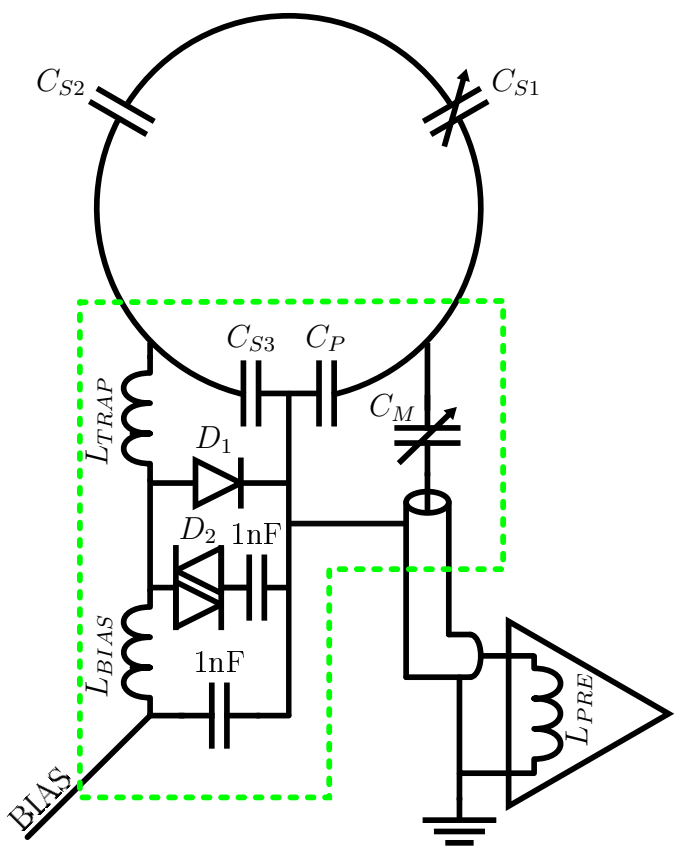


Figure 4-1: Complete loop circuit schematic

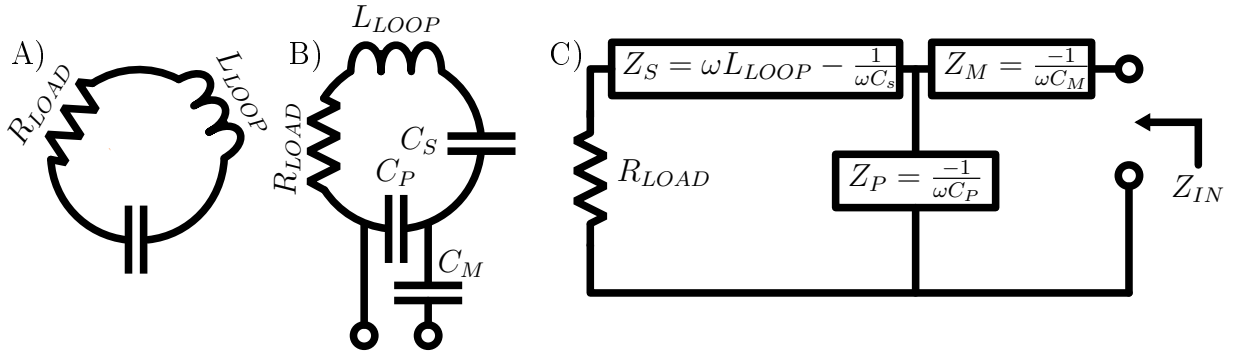


Figure 4-2: Loop circuit models.

4.4 Complete Loop Circuit

Figure 4-2B shows the creation of an output port in the loop circuit. The total loop capacitance is split into C_P , across which the output port is formed, and C_S . A series capacitor C_M is added to one terminal of the output port. In the first part of the following analysis, grouping components values into the block impedances defined in eq. 4.1 and fig. 4-2C results in clearer and more compact expressions, so I have made that substitution.

$$\begin{aligned} X_S(\omega) &= \omega L_{LOOP} - \frac{1}{\omega C_S} \\ X_P(\omega) &= \frac{-1}{\omega C_P} \\ X_M(\omega) &= \frac{-1}{\omega C_M} \end{aligned} \tag{4.1}$$

4.5 Loop Circuit Analysis

The loop circuit has an input impedance of Z_{IN} at its port, as defined in equation 4.2. This impedance can be split into its real and imaginary parts, R_{IN} and X_{IN} , shown in equations 4.3 and 4.4.

$$\begin{aligned} Z_{IN} &= (jX_p(\omega)) \parallel (jX_S(\omega) + R_{LOAD}) + jX_M(\omega) \\ &= \frac{jX_P(\omega)(jX_S(\omega) + R_{LOAD})}{j(X_P(\omega) + X_S(\omega)) + R_{LOAD}} + jX_M(\omega) \end{aligned} \tag{4.2}$$

$$R_{IN} = Re(Z_{IN}) = \frac{X_P(\omega)^2 R_{LOAD}}{R_{LOAD}^2 + (X_P(\omega) + X_S(\omega))^2} \quad (4.3)$$

$$X_{IN} = Im(Z_{IN}) = \frac{X_P(\omega)(R_{LOAD}^2 + X_S(\omega)(X_P(\omega) + X_S(\omega)))}{R_{LOAD}^2 + (X_P(\omega) + X_S(\omega))^2} + X_M(\omega) \quad (4.4)$$

4.6 Loop Component selection

4.6.1 Loop Circuit Considerations

Minimizing Preamp Noise Figure

The vendor supplied preamplifier is designed to achieve minimum noise figure when presented with a purely real 50Ω load at its input. Therefore, component values should be selected such that $R_{IN} = 50\Omega$ and $X_{IN} = 0\Omega$. Call this optimal input impedance $Z_{IN_{OPT}}$.

Preamp Decoupling

Preamp decoupling is usually achieved by resonating a capacitor in the loop (C_P in figure 4-2) with an inductor in series with one terminal of the output port (in the same position as C_M in figure 4-2) through the input of the preamplifier. In our case, however, the inductance is integrated into the preamplifier itself. I measure the inductance of the preamplifier input to be roughly $130nH$ at $123.25MHz$. The details of the preamp topology are unavailable to me, so I simply consider it to have an impedance of $Z_{PRE} = j\omega L_{PRE}$, which is transformed to Z_{PRE}' (as shown in equation 4.5) by the short length of coaxial cable (with characteristic impedance Z_0) connecting the preamp to the loop.

$$Z_{PRE}'(\omega) = Z_0 \cdot \frac{Z_{PRE}(\omega) - jZ_0 \cdot \tan(2\pi \cdot \frac{L_{COAX}}{\lambda})}{Z_0 - jZ_{PRE}(\omega) \cdot \tan(2\pi \cdot \frac{L_{COAX}}{\lambda})} \quad (4.5)$$

$$X_{PRE}'(\omega) = \text{Im}(Z_{PRE}'(\omega)) \quad (4.6)$$

In any case, preamp decoupling is achieved when C_P , C_M , and the transformed preamp input impedance resonate together, as defined in equation 4.7.

$$X_P(\omega) + X_M(\omega) + X_{PRE}'(\omega) = 0 \quad (4.7)$$

4.6.2 Loop Resonance

I define loop resonance as occurring when $X_P + X_S = 0$, at a frequency of ω_0 (eq. 4.8). In this case, the equations for R_{IN} and X_{IN} simplify to equations 4.9 and 4.10 respectively. One can begin to see how components could be selected to set $R_{IN}|_{\omega=\omega_0} = \text{Re}(Z_{IN_{OPT}})$, but with the topology we've selected it is impossible to achieve $X_{IN}|_{\omega=\omega_0} = 0$. You could do both if you changed C_M to an inductor, but then it becomes impossible to meet the preamp decoupling condition (eq. 4.7).

$$\omega_0 = \sqrt{\frac{C_P + C_S}{C_P C_S L_{LOOP}}} \quad (4.8)$$

$$R_{IN}|_{\omega=\omega_0} = \frac{C_S L_{LOOP}}{R_{LOAD} C_P (C_P + C_S)} \quad (4.9)$$

$$X_{IN}|_{\omega=\omega_0} = -\sqrt{\frac{C_S L_{LOOP}}{C_P (C_P + C_S)}} \cdot \frac{C_M + C_P}{C_M} \quad (4.10)$$

4.6.3 Off resonance behavior

It is not necessary that the loop be tuned to resonate precisely at the frequency of interest. The position of ω_0 relative to that of the Lamor frequency ω_L is another variable that we can manipulate to achieve the desired loop circuit characteristics.

Capacitive Divider Ratio

Consider choosing C_P and C_S to achieve loop resonance at a frequency a factor α away from ω_L , so that $\omega_0 = \alpha \cdot \omega_L$. We can quickly eliminate C_S from eq. 4.8. Whatever C_P , α , and ω_L we choose will imply eq. 4.11 for C_S .

$$C_S(C_P, \alpha, \omega_L) = \frac{C_P}{C_P L_{LOOP} \alpha^2 \omega_L^2 - 1} \quad (4.11)$$

Plugging eq. 4.11 into eq. 4.3, then solving $R_{IN} = Z_{IN_{OPT}}$ for C_P , we get eq. 4.12.

$$C_P(\alpha, \omega_L) = \frac{1}{\omega_L} \sqrt{\frac{R_{LOAD}}{Z_{IN_{OPT}}(R_{LOAD}^2 + (\alpha^2 - 1)^2 \omega_L^2 L_{LOOP}^2)}} \quad (4.12)$$

Choosing α and C_M

The only remaining free parameters are α and C_M . They must be chosen to achieve purely real input impedance ($X_{IN} = 0$) and preamp decoupling ($X_P(\omega_L) + X_M(\omega_L) + X_{PRE}'(\omega_L) = 0$). Plugging in C_S and C_P from above into these two requirements results in a system of equations 4.13. Constraining α to be positive, this system has single solution: α as in eq. 4.14 and C_M as in eq. 4.15.

$$\begin{cases} \frac{-1}{\omega_L C_M} + \frac{(\alpha^2 - 1)\omega_L L_{LOOP} Z_{IN_{OPT}}}{R_{LOAD}} - \frac{1}{\omega_L C_P(\alpha, \omega_L)} = 0 \\ \frac{-1}{\omega_L C_M} + \omega_L L_{PRE} - \frac{1}{\omega_L C_P(\alpha, \omega_L)} = 0 \end{cases} \quad (4.13)$$

$$\alpha = \sqrt{1 + \frac{L_{PRE} R_{LOAD}}{L_{LOOP} Z_{IN_{OPT}}}} \quad (4.14)$$

4.6.4 Optimal Component values

With α uniquely determined, C_M , C_P , and C_S are each fully constrained. Our final component value formulas are shown in eq. 4.15.

$$\begin{aligned}
C_M &= \frac{1}{\omega_L} \cdot \frac{1}{\omega_L L_{PRE} - \sqrt{\frac{R_{LOAD}}{Z_{IN_{OPT}}}(\omega_L^2 L_{PRE}^2 + Z_{IN_{OPT}}^2)}} \\
C_P &= \frac{1}{\omega_L} \cdot \frac{1}{\sqrt{\frac{R_{LOAD}}{Z_{IN_{OPT}}}(\omega_L^2 L_{PRE}^2 + Z_{IN_{OPT}}^2)}} \\
C_S &= \frac{1}{\omega_L} \cdot \frac{1}{\omega_L(L_{PRE}\frac{R_{LOAD}}{Z_{IN_{OPT}}} + L_{LOOP}) - \sqrt{\frac{R_{LOAD}}{Z_{IN_{OPT}}}(\omega_L^2 L_{PRE}^2 + Z_{IN_{OPT}}^2)}}
\end{aligned} \tag{4.15}$$

4.6.5 Verifying Optimal Component Values

Figure 4-3 illustrates the success of this component selection strategy in simultaneously achieving optimal input impedance and preamp decoupling. The impedance plots shown are based on estimated parameters of a loop in the belly panel. Numerical values for this simulation are summarized in tables 4.1 and 4.2.

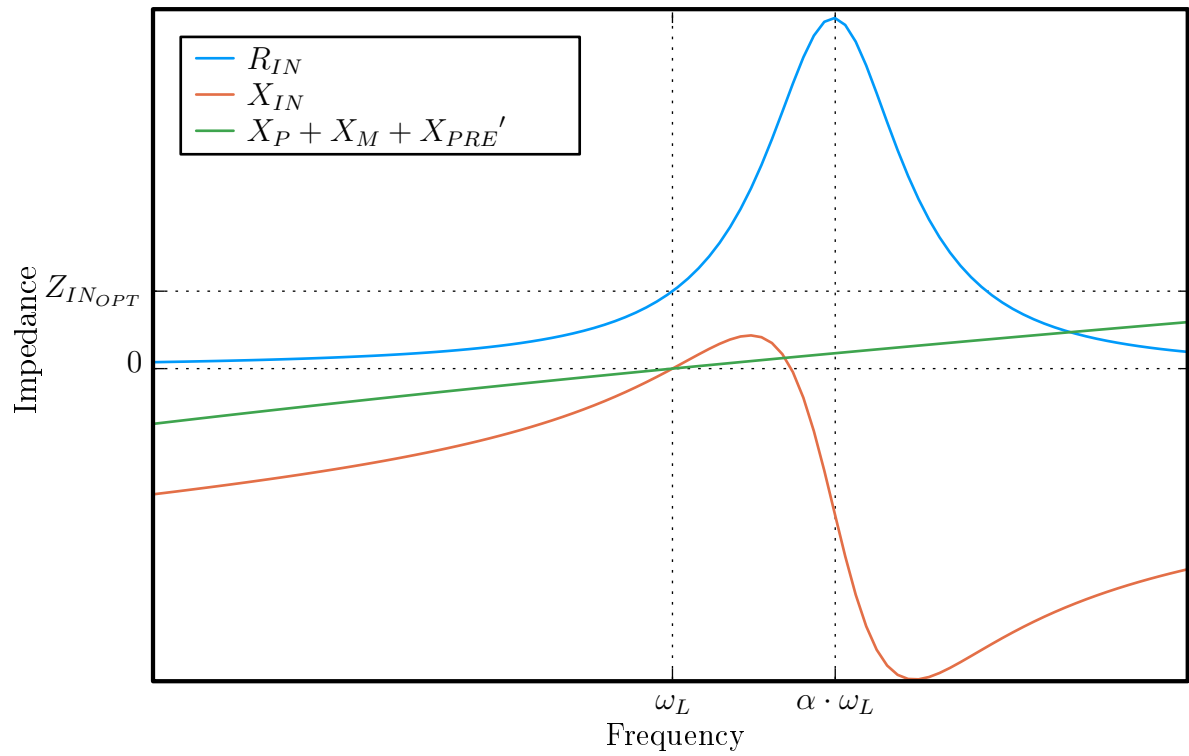


Figure 4-3: Loop impedances vs. frequency with optimal component values.

Table 4.1: Loop simulation parameters

Parameter	Value
R_{LOAD}	10Ω
L_{LOOP}	$247nH$
L_{PRE}	$130nH$
Z_{INOPT}	50Ω
ω_L	$123.25MHz$

Table 4.2: Calculated optimal component values

Parameter	Value
C_M	$25.8pF$
C_P	$25.8pF$
C_S	$8.0pF$
α	1.051

Chapter 5

Figures of Merit

The aim of this project was to create a custom coil that performs better than existing arrays in a particular application. Our primary means of evaluating relative performance is direct comparison of two related performance metrics: SNR maps and SENSE geometry factor (g-factor) maps. A brief discussion of each follows. For a complete treatment, see the original SENSE paper: [6].

5.1 Signal to Noise Ratio Maps

In MRI, SNR is commonly defined as the ratio between signal amplitude and the standard deviation of noise. The MR signal to noise ratio provided by any coil or coil array varies as a function of space. A heatmap of SNR in absolute SNR units as defined by Kellman and McVeigh [3] in a given plane is a useful visual tool that can be used to judge whether a coil is well suited to imaging in a particular region of interest such as the fetal brain or placenta. An SNR map is easy to generate for a single coil. One can simply run an imaging sequence with intrinsically high SNR twice; once with an initial RF excitation and once without. The first sequence should produce an image that is dominated by the MR signal, and the second sequence produces a noise only image. A SNR map in conventionally defined SNR units is obtained by dividing the first image by the standard deviation of the noise only image.

Generating SNR maps for multi coil arrays is less straightforward, and depends

on the method used to combine data from individual elements. The Roemer paper [8] describes an optimal way of combining array coil data in the spatial domain that results in maximum SNR and normalized noise intensity in every voxel of the resulting image. First, a complete image is acquired and reconstructed from every element in the array. Next, a sample of pure noise data is acquired to generate a channel noise covariance matrix Ψ , of which a single element Ψ_{ij} is the noise covariance between receivers i and j .

Now, the individual coil images are combined on a voxel by voxel basis. For a single voxel, arrange the values S_i of that voxel in each of the individual coil images in a vector S . Similarly, arrange the sensitivities of each coil to the voxel under consideration in a vector C . The matrix equation for the voxel intensity in the optimal SNR uniform noise image is then eq. 5.1. If the individual coil images have sufficiently high SNR, then S serves as a good approximation of C , and equation 5.1 simplifies to 5.2. If it is assumed that there is no noise correlation between distinct channels and that all channels are identically loaded, Ψ becomes proportional to the identity matrix, and the optimal SNR formula simplifies to 5.3. This is equivalent to summing the squared magnitudes of the uncombined images, then taking the square root of the result.

$$I_{OPT} = \frac{C^H \Psi^{-1} S}{\sqrt{C^H \Psi^{-1} C}} \quad (5.1)$$

$$I_{COV} = \sqrt{S^H \Psi^{-1} S} \quad (5.2)$$

$$I_{RSOS} = \sqrt{S^H S} \quad (5.3)$$

SNR Map Equations

As stated, the optimal combination method is constructed to create a uniform noise image, where every voxel in the final image has unity noise standard deviation. So, the expression for a voxel in an optimal combination method SNR map is the same

as the expression for a voxel in the image:

$$SNR_{COV} = I_{COV} = \sqrt{S^H \Psi^{-1} S} \quad (5.4)$$

For the RSOS method, the SNR map is calculated as:

$$SNR_{RSOS} = \frac{S^H S}{\sqrt{S^H \Psi S}} \quad (5.5)$$

5.2 SENSE Geometry Factor

5.2.1 K-space Sampling for the 2DFT

The basic Fourier abstraction used in traditional 2D MRI with Cartesian k-space sampling illuminates a fundamental constraint on imaging speed: k-space traversal speed.

Sampling Constraints

The spatial extents of an image dictate the spectral spacing of samples that must be acquired to encode it with the DFT [5]. In order to 2D Fourier encode an image of width FOV_x and height FOV_y , k-space samples must be spaced $\frac{1}{FOV_X}$ apart in the k_x direction and $\frac{1}{FOV_Y}$ apart in the k_y direction, as defined in eq. 5.6.

$$\begin{aligned} FOV_x &= \frac{1}{\delta k_x} \\ FOV_y &= \frac{1}{\delta k_y} \end{aligned} \quad (5.6)$$

The spatial resolution of an image dictates the extents of spectral data that must be acquired to encode it with the DFT. In order to 2D Fourier encode an image with voxels δ_x wide and δ_y tall, data must be sampled over a period of approximately $\frac{1}{\delta_x}$ in the k_x direction and $\frac{1}{\delta_x}$ in the k_y direction, as defined in eq. 5.7.

$$\begin{aligned}\delta_x &\approx \frac{1}{2k_{xmax}} \\ \delta_y &\approx \frac{1}{2k_{ymax}}\end{aligned}\tag{5.7}$$

It is clear that the number k-space samples needed to resolve an image grows linearly with both FOV and voxel density, and that the maximum extents of those samples in k-space increases linearly with voxel density. K-space is sampled by traversing a continuous path that sequentially visits the coordinates of each sample. The maximum speed of k-space traversal is fundamentally limited by patient safety considerations and technological limitations. So, for a given maximum speed and optimum path, there is a minimum acquisition time for a fully sampled 2DFT sequence with a given FOV and spatial resolution.

Cartesian Undersampling

An imaging sequence can be accelerated by skipping some points in k-space, then attempting by some means to reconstruct a complete image from incomplete k-space data. In the case of cartesian sampling for the 2DFT, a natural strategy is to regularly skip entire lines of k-space data in one dimension [6], for example acquiring every other line ($R=2$) or every third line ($R=3$). The effect of this regular undersampling strategy is to effectively increase δ by a factor of R , and to accordingly decrease *FOV* by the same factor of R . This causes parts of the object being imaged that lie outside of the reduced FOV to wrap around the edges of that FOV and alias onto other voxel positions.

SENSE

The Pruessmann paper [6] introduced the strategy of "Sensitivity Encoding" as a means of undoing the aliasing induced by undersampling. In an array coil, different receive elements have different spatial sensitivity profiles. These varying sensitivities provide different "views" of the same aliased image, and this extra information is used to unfold the aliased image on a pixel by pixel basis.

Consider an array with n_C individual elements, each with a unique view of a voxel location that, in the reduced FOV image, represents a superposition of n_P physical voxel locations. A sensitivity matrix S is constructed to describe the sensitivity of each receive element to each of the voxel positions that are aliased into a single pixel in the final image. An individual element $S_{\gamma,\rho}$ in this matrix represents the sensitivity of receive element number γ to superimposed pixel number ρ . The values of the voxel in the reduced FOV images from each receive element are arranged in a vector \vec{a} of length n_C . Similar to in the previous section, a $n_C \times n_C$ receiver noise covariance matrix Ψ is constructed from a noise-only acquisition. The unfolding matrix is then:

$$U = (S^H \Psi^{-1} S)^{-1} S^H \Psi^{-1} \quad (5.8)$$

The vector of image values in the n_p voxels of the unaliased image are estimated by:

$$\vec{v} = U \vec{a} \quad (5.9)$$

This unfolding process is repeated for every voxel in the reduced FOV image.

SENSE g-factor

By accelerating an image acquisition by a factor of R , we expect that the SNR of the resulting image must correspondingly decrease by a factor of $\frac{1}{\sqrt{R}}$ [5]. Usually, though, imperfect conditioning of the sensitivity matrix results in a steeper SNR penalty. The extent to which SENSE underperforms the best case SNR penalty is characterized by the geometry factor, or g-factor, defined in eq. 5.10. The g-factor varies as a function of space, and is defined for each voxel in the full FOV image. It is called the geometry factor because it depends largely on the geometry of the receive array. When more independent views of an aliased pixel are available, a higher acceleration factor can be attempted without poor conditioning amplifying noise to an unacceptable degree. This is the mission of the array coil.

$$g_{SENSE} = \frac{1}{\sqrt{R}} \cdot \frac{SNR_{FULL}}{SNR_{ACCEL}} \quad (5.10)$$

Plots of 2D SENSE g-factor maps in a given slice are a useful graphical tool for assessing the ability of an array to support a given acceleration factor along a particular dimension (or, along two dimensions simultaneously.) SENSE g-factor is widely used to compare the acceleration capability of different coil arrays because it is straightforward to compute and gives insights into the fundamental ability of an array to enable acceleration using any method. Still, it is important to note that unique formulations of g-factor have been developed for other acceleration methods, such as SMASH and GRAPPA [1].

Chapter 6

Methods

6.1 Bench Tests

6.1.1 Intercoil Coupling and Reflection Coefficient Measurements

A network analyzer connected directly to loop output ports was used to measure coupling between neighboring coil elements (S_{12}), and to measure individual coil output reflection coefficients (S_{11}). For each of these tests, the output power of the network analyzer was reduced to -25dBm and the coil was appropriately loaded by a test phantom. This test configuration was used during the iterative geometric decoupling adjustment process, where the loops are manually bent and reconfigured to minimize neighbor-to-neighbor coupling.

6.1.2 Loop Detuning and Preamp Decoupling Verification

The active detune capability and preamp decoupling performance were tuned and characterized using a pair of decoupled ($S_{12} < 70dB$) inductive probes loosely coupled to the loop under test. In this arrangement, the S_{12} measurement between the two probes is directly proportional to the current flowing in the loop [7]. Both the active detune capability and preamplifier decoupling strategy work by introducing a second

resonance near the loop resonance frequency, which "splits" the loop resonance into two peaks above and below the initial resonance frequency. The null between these peaks is moved to ω_L by adjustment of a tunable component. For the active detune strategy, this tunable component is an adjustable air-core inductor (L_{TRAP} in fig. 4-1). For preamp decoupling, it is a trim capacitor (C_M in fig. 4-1).

6.2 MRI Data Acquisition and Reconstruction

Images of the pregnant abdominal phantom were acquired for using both the 64 channel fetal coil and the standard combination of 16 channels from a 32 channel spine array and all channels from an 18 channel flexible body array. Three orthogonal slices (transverse, coronal, and sagittal) intersecting the fetal brain compartment were carefully duplicated using both array configurations. An extremely high SNR PD weighted 2DGRE sequence ($TR = 3500ms, TE = 4ms, FA = 45^\circ, FOV = 400mm, \delta \approx 2mm \times 2mm \times 7mm, BW = 180Hz/px$) was chosen so that each of the uncombined coil images has decent SNR (> 20) in the deep central region of the fetal brain compartment, and thus can be taken as an accurate approximation of a coil sensitivity map [8]. The same sequence was run with the reference TX voltage set to 0V to acquire noise-only data for the generation of a noise covariance matrix Ψ . Data were acquired on a 3T Magnetom Skyra System (Siemens Healthcare, Erlangen, Germany).

Covariance weighted SNR maps and SENSE g-factor maps were computed offline using the resulting raw data. For the fetal coil, single channel SNR maps were generated by dividing each of the 64 uncombined coil images by the standard deviation of a corresponding noise only image. The mean value of each single channel SNR map was computed inside an ROI ($A = 29$ voxels) in the fetal brain region of the anthropomorphic phantom as a means of assessing the relative importance of each component in the array geometry.

Chapter 7

Results

7.1 Covariance Weighted SNR Maps

Covariance weighted SNR maps for three perpendicular slices chosen to intersect the fetal brain compartment are shown in figs. 7-1, 7-2, and 7-3. In each cross section, it can be seen that the fetal array provides greatly increased SNR in the periphery of the phantom, but only narrowly outperforms the standard array configuration in the deep central region where the fetus is actually located. In this particular dataset, SNR was improved by approximately 5% inside the fetal brain compartment in each of the three slices.

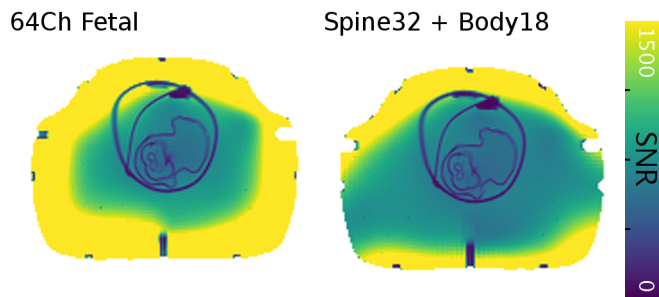


Figure 7-1: Comparative covariance weighted SNR maps, transverse slice through fetal phantom brain.

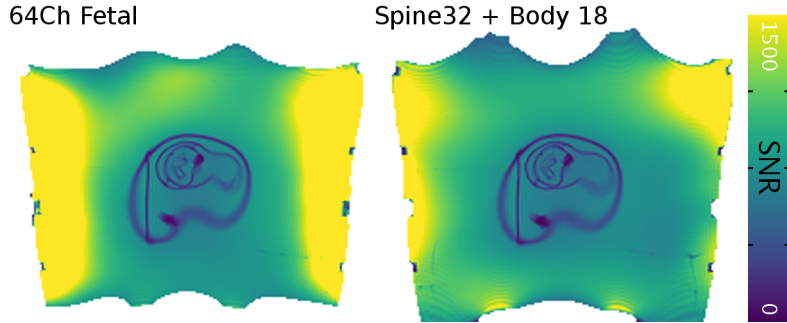


Figure 7-2: Comparative covariance weighted SNR maps, coronal slice through fetal phantom brain.

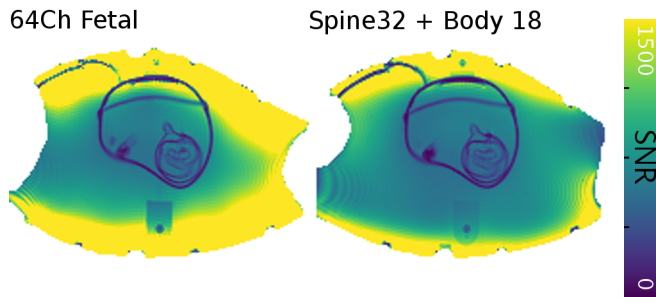


Figure 7-3: Comparative covariance weighted SNR maps, sagittal slice through fetal phantom brain.

7.2 Inverse G-Factor Maps

As compared to the standard combination of the 32 channel spine array and 18 channel flexible body array, the 64 channel fetal coil allows increase in SENSE acceleration factor from four to five in the right-left direction (figs. 7-4, 7-6) and 3 to 4 in the head-foot direction (figs. 7-7, 7-8) while maintaining acceptably low noise amplification levels. Both array configurations have poor acceleration capability in the anterior-posterior direction (figs. 7-5, 7-9). Note that in order to increase contrast in the relevant range, the color scale on these maps goes from 0.5 to 1, not 0 to 1.

Figure 7-10 shows inverse SENSE g-factor maps for 2D acceleration in the head-foot and left-right directions, comparing array performance at $R = (3, 4)$ and $R = (4, 5)$. This comparison was chosen to highlight the best case improvement in acceleration capability provided by the fetal coil. Inside a large central ROI covering the entire fetus, the fetal coil maintains $g \leq 1.5$ with $R = 4, 5$ while the product array

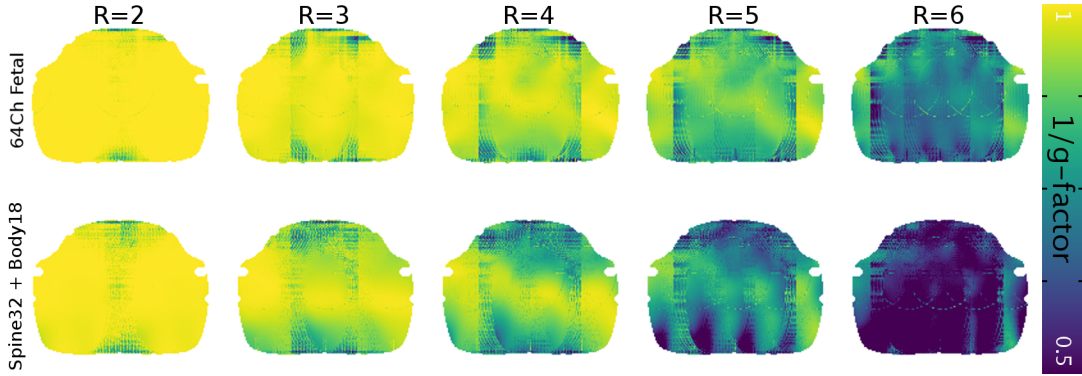


Figure 7-4: Comparative inverse SENSE g-factor maps, transverse slice through fetal phantom brain, acceleration in right-left direction.

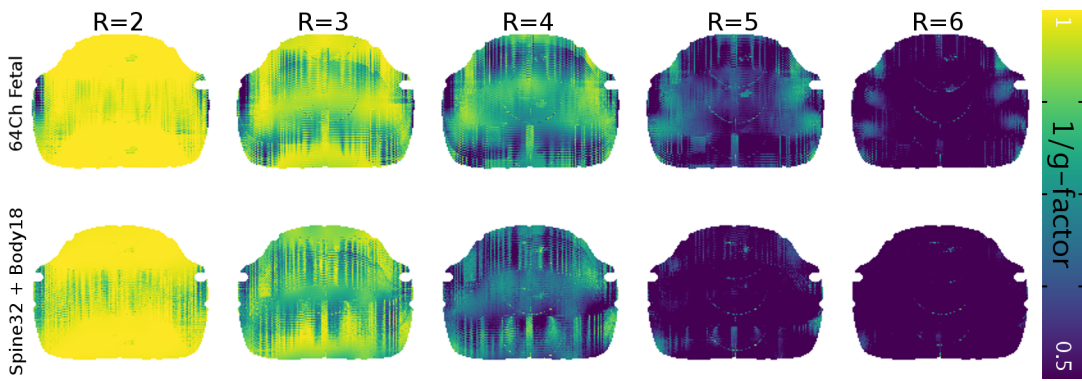


Figure 7-5: Comparative inverse SENSE g-factor maps, transverse slice through fetal phantom brain, acceleration in anterior-posterior direction.

only achieves $g \leq 3.9$. In the same ROI, they have mean inverse g-factors ($1/g$) of 0.82 and 0.43, respectively. Roughly speaking, the fetal coil has noise amplification levels at $R = (4, 5)$ that are comparable to the standard array configuration at $R = (3, 4)$. This represents a 67% increase in overall acceleration factor.

7.3 Noise Matrices

Figure 7-11 shows the absolute value of a noise covariance matrix Ψ calculated from this dataset. Figure 7-12 shows the same data normalized along the diagonal so that the element with indices j, k is the correlation coefficient for channels j and k . The correlation coefficient is equal to 1 when $j = k$.

The average off diagonal correlation coefficient is 0.051, and the maximum is 0.38.

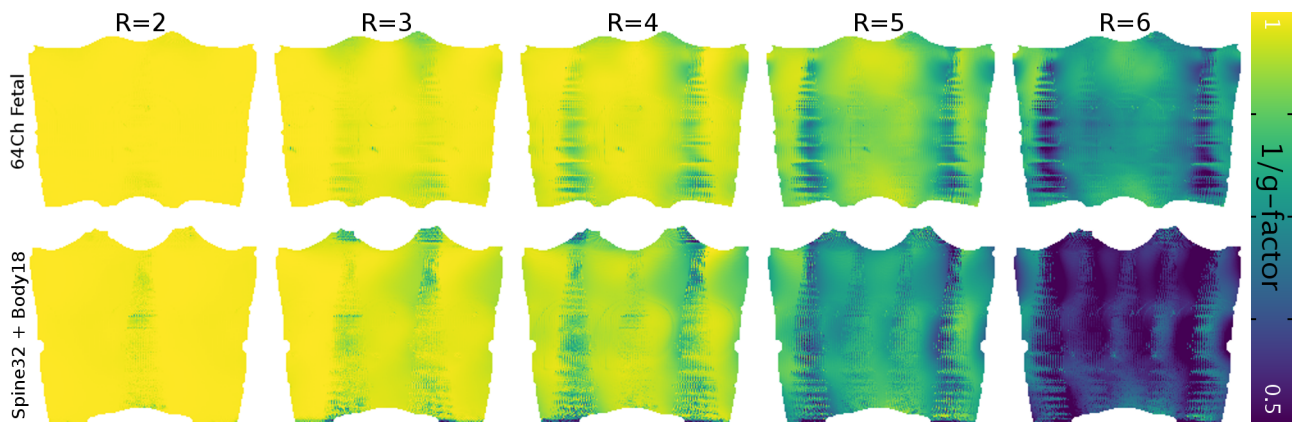


Figure 7-6: Comparative inverse SENSE g-factor maps, Coronal slice through fetal phantom brain, acceleration in right-left direction.

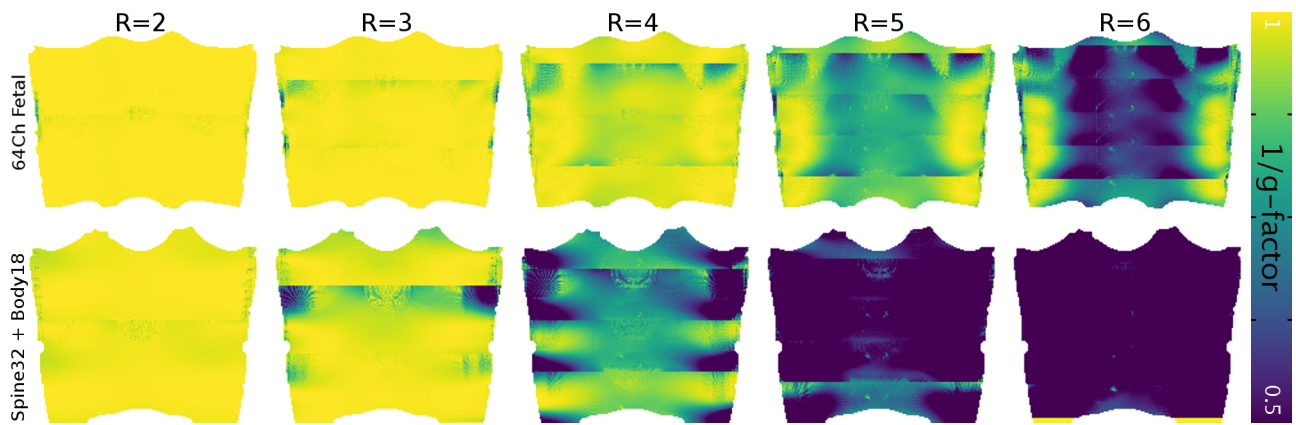


Figure 7-7: Comparative inverse SENSE g-factor maps, coronal slice through fetal phantom brain, acceleration in head-feet direction.

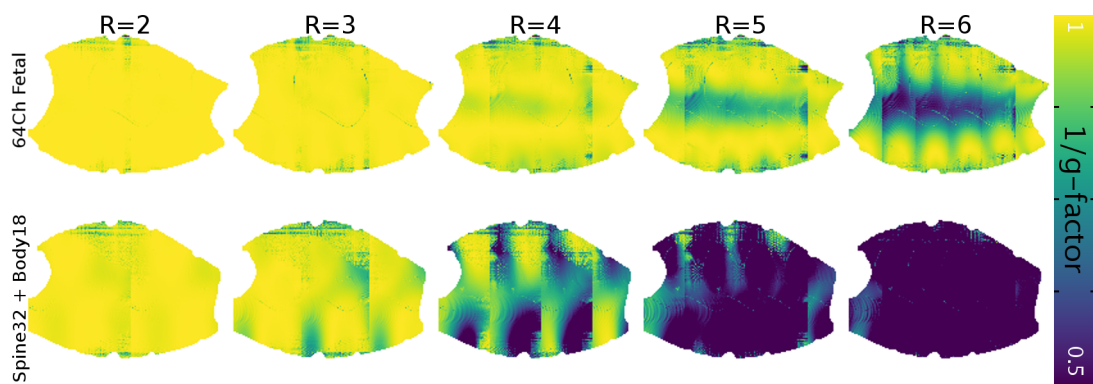


Figure 7-8: Comparative inverse SENSE g-factor maps, sagittal slice through fetal phantom brain, acceleration in head-feet direction.

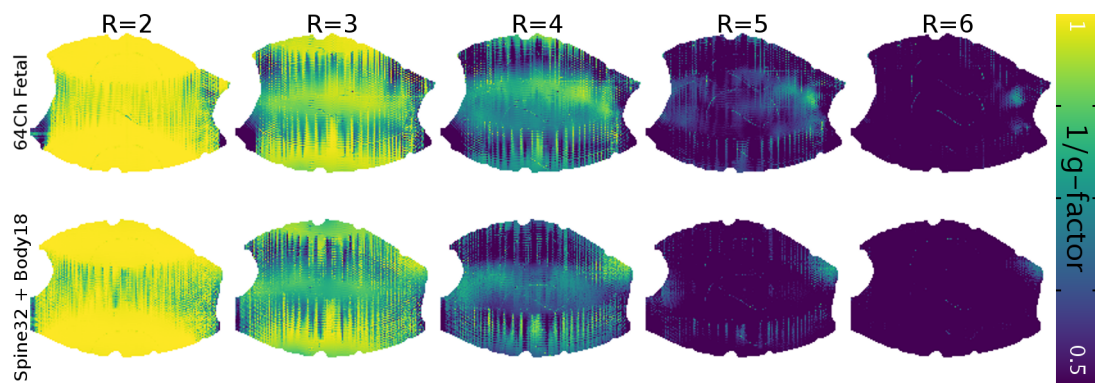


Figure 7-9: Comparative inverse SENSE g-factor maps, sagittal slice through fetal phantom brain, acceleration in anterior-posterior direction.

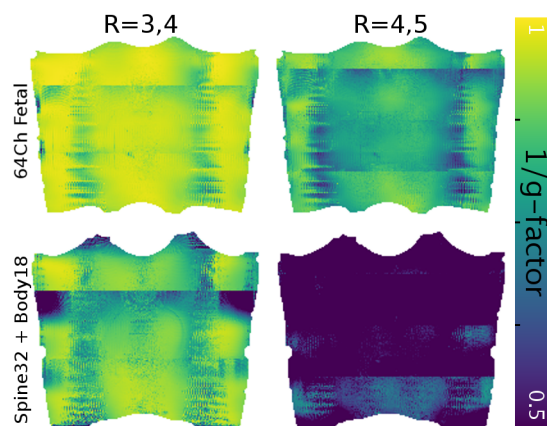


Figure 7-10: Comparative inverse SENSE g-factor maps, coronal slice through fetal phantom brain, acceleration in head-feet, right-left directions.

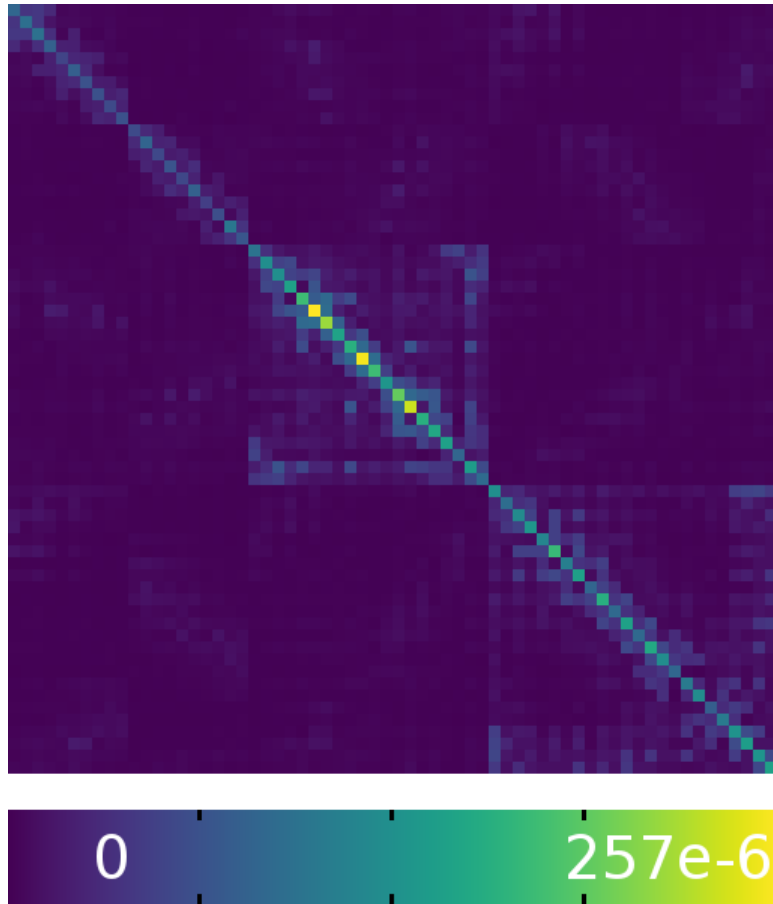


Figure 7-11: Absolute value of noise covariance matrix ($|\Psi|$).

Looking at the correlation coefficient matrix, several clearly defined regions of moderate correlation are apparent, with almost no correlation between different regions. The groupings follow the separation of elements into different array panels. From top left to bottom right, we see channels from the right side wing, left side wing, abdomen panel, and back panel.

7.4 Per-Element SNR

Figure 7-13 is a 1:4 scale diagram of the actual loop geometry used in the fetal array. Displayed inside each loop is the mean SNR of that channel inside the fetal brain ROI. It can be seen that elements in the back panel contributed most to overall SNR in the fetal brain compartment, followed by the belly panel and side wings.

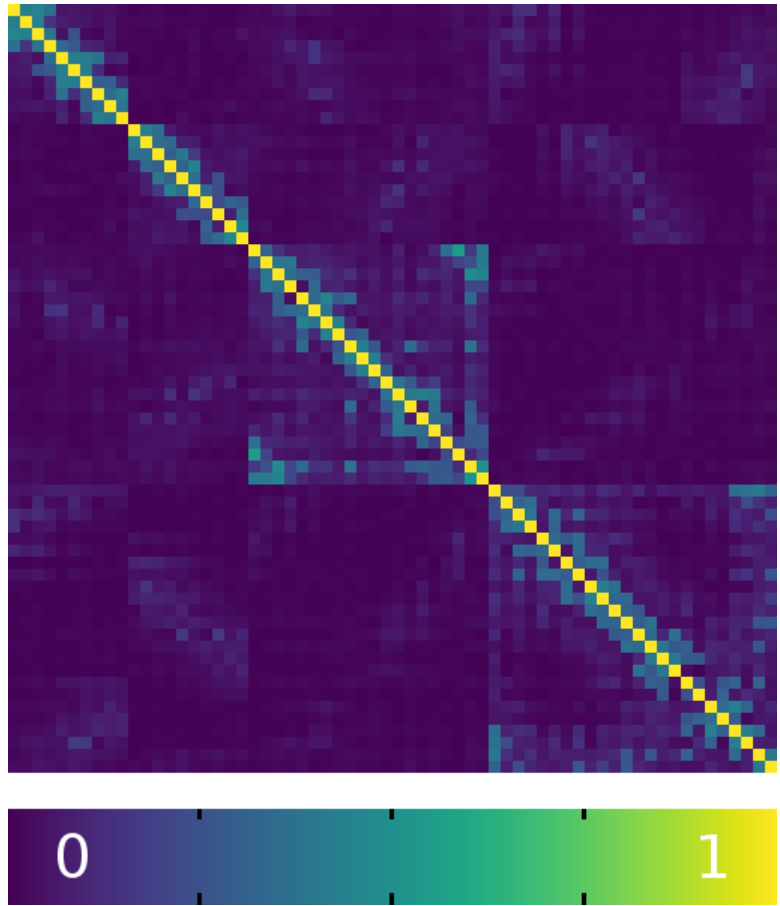


Figure 7-12: Absolute value of inter-channel noise correlation coefficients ($|\sqrt{\text{diag}(\Psi)}^{-1} \cdot \Psi \cdot \sqrt{\text{diag}(\Psi)}|$).

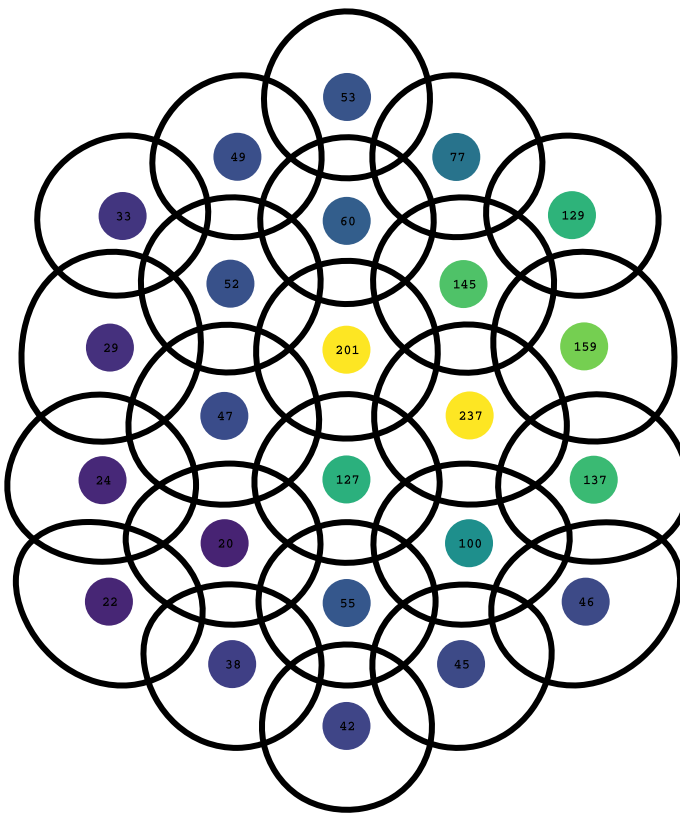
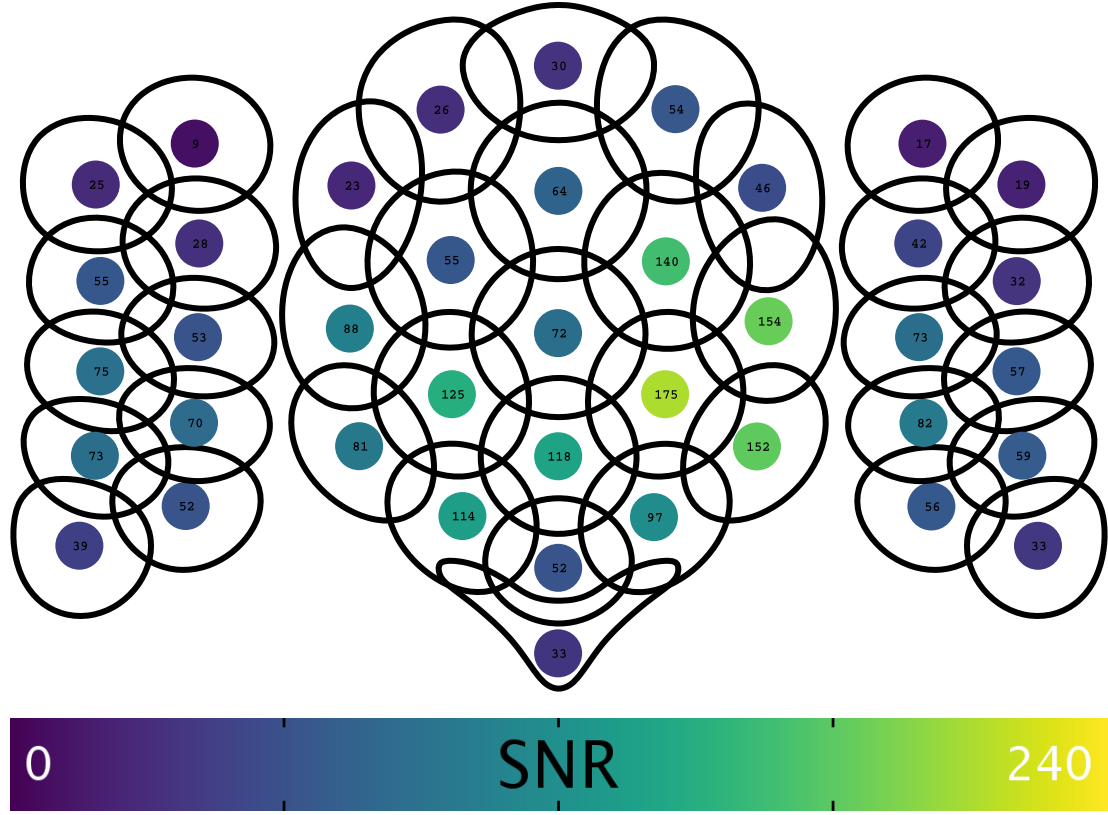


Figure 7-13: Mean Single Element SNR values Inside the Fetal Phantom Brain
(Top:Abdomen Panel and Side Wings, Bottom: Back panel)

Chapter 8

Discussion

The modest SNR improvement seen in unaccelerated imaging is likely attributed to the deep (nearly central) location of the fetal head where coil arrays with more than 16 elements already approach the ultimate SNR available [9]. Nonetheless, because the SNR is achieved with array elements with higher spatial frequency content sensitivity profiles, there is an improvement in acceleration capability.

The anterior and posterior array panels contribute overwhelmingly to the overall SNR in the fetal brain. Acceleration capability in the anterior-posterior direction was not substantially improved beyond what would be expected with just the two views of the phantom provided by anterior and posterior panels. The side wings do, however, benefit acceleration in the right-left direction.

Due to delays in IRB approval and subject recruitment, the array has thus far only been tested on the purpose built pregnant abdomen phantom. The phantom and array were designed based on the same segmented models of a pregnant volunteer, and so by design the coil fits the phantom very well. Since this close fit is one of the noted advantages of the 22 week fetal coil, further testing on a varied population of pregnant volunteers is needed to fully assess any performance improvement. Furthermore, practical considerations like patient comfort have not yet been evaluated.

Bibliography

- [1] Felix A. Breuer, Stephan A R Kannengiesser, Martin Blaimer, Nicole Seiberlich, Peter M. Jakob, and Mark A. Griswold. General formulation for quantitative G-factor calculation in GRAPPA reconstructions. *Magnetic Resonance in Medicine*, 62(3):739–746, 2009.
- [2] D. I. Hoult and Paul C. Lauterbur. The sensitivity of the zeugmatographic experiment involving human samples. *Journal of Magnetic Resonance (1969)*, 34(2):425–433, 1979.
- [3] Peter Kellman and Elliot R. McVeigh. Image reconstruction in SNR units: A general method for SNR measurement. *Magnetic Resonance in Medicine*, 54(6):1439–1447, 2005.
- [4] T.H. Lee. *The Design of CMOS Radio-Frequency Integrated Circuits*. Cambridge University Press, 2004.
- [5] Dwight G. Nishimura. *Principles of magnetic resonance imaging*. 1.1 edition, 2010.
- [6] Klaas P Pruessmann, Markus Weiger, Markus B Scheidegger, and Peter Boesiger. SENSE: Sensitivity encoding for fast MRI. *Magnetic Resonance in Medicine*, 42(5):952–962, 1999.
- [7] Arne Reykowski, Steven M. Wright, and Jay R. Porter. Design of Matching Networks for Low Noise Preamplifiers. *Magnetic Resonance in Medicine*, 33(6):848–852, 1995.
- [8] P. B. Roemer, W. A. Edelstein, C. E. Hayes, S. P. Souza, and O. M. Mueller. The nmr phased array. *Magnetic Resonance in Medicine*, 16(2):192–225, 1990.
- [9] Florian Wiesinger, Peter Boesiger, and Klaas P. Pruessmann. Electrodynamics and ultimate SNR in parallel MR imaging. *Magnetic Resonance in Medicine*, 52(2):376–390, 2004.